NANO LETTERS

pubs.acs.org/NanoLett Letter

Orientation-Dependent Thermal Morphological Evolution of α-Fe Nanopillars

Longqi Bai, Longchao Huang, Yan Ma, Degang Xie,* and Zhiwei Shan

Cite This: *Nano Lett.* 2026, 26, 8551−8558 Read Online

ACCESS | Metrics & More | Article Recommendations | Supporting Information

ABSTRACT: One-dimensional nanostructures are typically single-crystalline, yet the mechanisms by which crystallographic orientation governs their thermal morphological evolution, a process that critically dictates their structural integrity and functional performance in high-temperature applications, remain poorly understood. Here, by observing the shape evolution of single-crystalline α-Fe nanopillars near 0.48 of the melting temperature, we show that increasing axial index results in stronger spheroidization and faster shortening. This behavior originates from a coupled thermodynamic-kinetic effect. On low-index axial pillars, strong effective surface-energy anisotropy stabilizes {100} and {110} facets, while limited adatom generation on these facets slows surface diffusion and shortening. In contrast, geometric constraints on high-index axial pillars promote the exposure of high-index facets, reducing effective surface-energy anisotropy and facilitating adatom formation, thereby accelerating spheroidization and shortening. These results identify axial orientation as a key parameter governing the thermal evolution pathway of one-dimensional nanostructures and provide design principles for engineering thermally robust nanoscale systems.

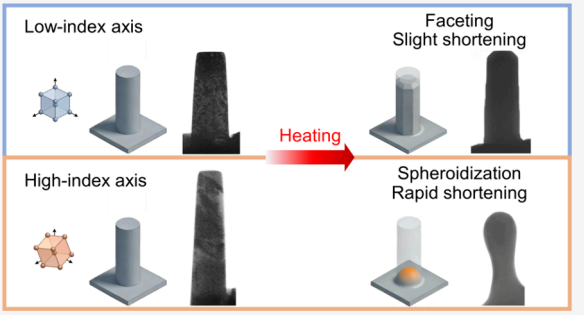

KEYWORDS: *Single-Crystalline α-Fe Nanopillars, Orientation-Dependent Thermal Evolution, Surface-Energy Anisotropy, Adatom-Mediated Mass Transport*

One-dimensional (1D) nanostructures are typically single-crystalline, with varying axial crystal orientations.[1−3] From a thermomechanical perspective, the 1D morphology is metastable and tends to undergo shape transformations once surface diffusivity becomes active, for example, at elevated temperatures. The operational reliability of advanced nanoscale devices, including sensors, catalytic systems and energy storage devices,[3−5] depends critically on the morphological stability of these nanostructures. Their shape, aspect ratio and surface orientation govern anisotropic magnetic, optical, thermal, electrical, mechanical and catalytic properties.[6−19] In applications, the high-temperature environments often activate surface diffusion, driving thermally induced morphological evolution that can degrade material performance. Understanding the thermal evolution of these nanostructures is therefore critical for optimizing their design and improving their reliability in real applications.

Previous investigations have documented a wide range of thermally induced shape transformations in 1D nanostructures,[10−22] yet the observed behaviors remain diverse and sometimes inconsistent. Two representative evolution modes are commonly identified: faceting, where the system reconstructs to expose specific low-energy facets (e.g., {100}, {110} in body-centered cubic structure),[23,24] and spheroidization, which minimizes total surface area.[23,25] In many cases, these transformations are accompanied by pronounced axial shortening or even fragmentation, raising critical concerns regarding structural stability. Although both modes originate from the thermodynamic driving force to minimize surface energy, the specific evolution pathway and the extent of transformation are governed by kinetic constraints. These constraints are strongly affected by crystallographic axial orientation, which determines the adatom formation and surface diffusion kinetics.[26,27] Several simulations have explored the orientation-dependent evolution of nanostructures.[28−31] For instance, molecular dynamics simulations revealed that square gold nanorods initially bounded by the {110} facets became rounded, while those bounded by the {100} facets exposed the {111} facets and transformed into rhombic shapes.[28,29] However, these studies primarily attributed pathway selection to the initial fraction of low-energy surface facets, and did not clarify the transition criteria or their sensitivity to axial orientation. Moreover, how orientation-dependent pathway selection influences the subsequent short-

Received: April 18, 2026
Revised: May 24, 2026
Accepted: June 15, 2026
Published: June 18, 2026

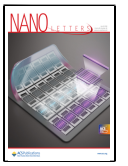

https://doi.org/10.1021/acs.nanolett.6c01885
Nano Lett. 2026, 26, 8551−8558

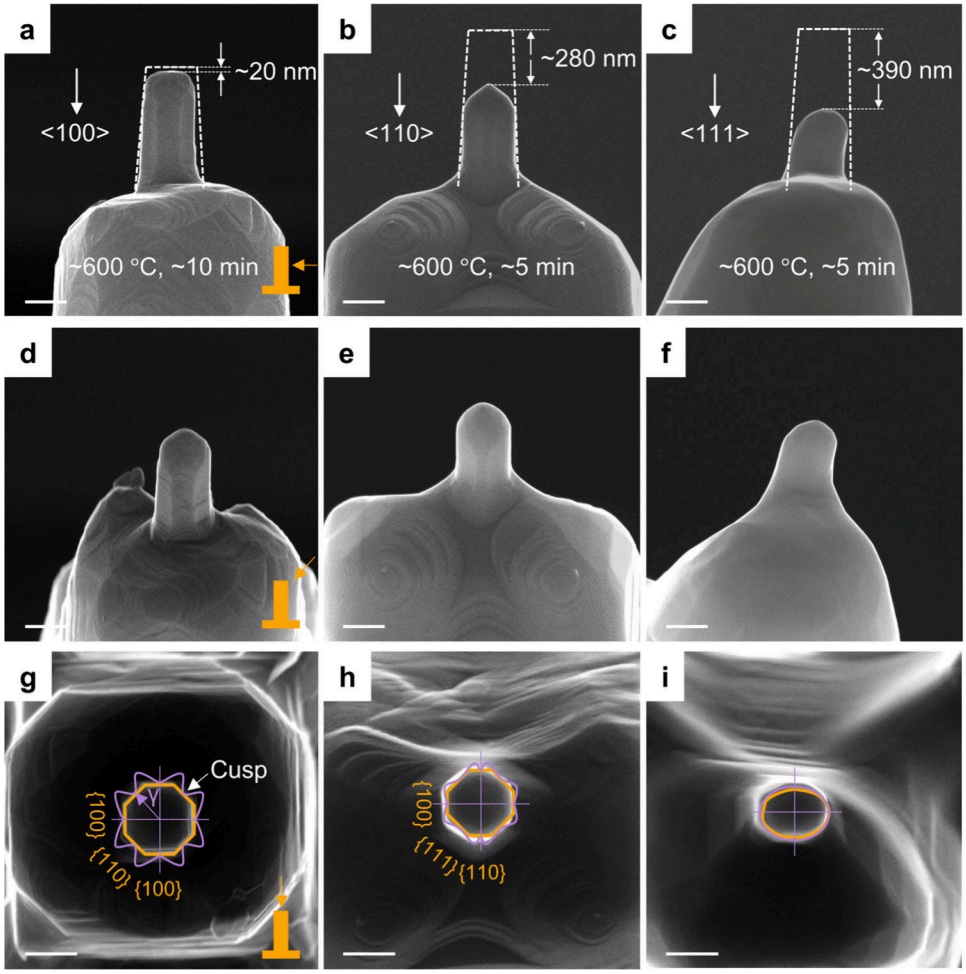

Figure 1. Comparison of morphological changes in α-Fe pillars with ⟨100⟩, ⟨110⟩ and ⟨111⟩ axial orientations after heating near 600 °C, viewed from the side (a–c), 45° (d–f) and the top (g–i), respectively. The preheating profiles and the reduction in height after heating are shown as the white dotted lines and the numbers in (a–c). Facets with recognizable Miller indices and schematic illustration of orientation-dependent effective surface-energy anisotropy for the three types of nanopillars are indicated in (g–i). All scale bars: 200 nm.

ening behavior remains unclear. A systematic experimental investigation is therefore required.

To address this gap, we investigate the thermal morphological evolution of single-crystalline α-Fe nanopillars using the *in situ* transmission electron microscopy (TEM) setup shown in Figure S1. α-Fe-based nanostructures are promising for applications in magnetic devices and catalysis.[6,7,32] Self-supported cylindrical nanopillars with axial orientations ranging from low-index to high-index were fabricated as the starting geometry using focused ion beam (FIB), as this configuration facilitates precise control over dimensions and crystallographic alignment and eliminates extrinsic interactions between nanowires/nanopillars and the supporting substrate.[33−36] All samples were heated to ~600 °C, corresponding to ~0.48 of the melting temperature (T_m), at a rate of 20 °C min^{-1} and subsequently held for continuous observation. This temperature was chosen to activate surface diffusion while maintaining sufficiently slow kinetics to reveal the evolution details. Under these conditions, a clear orientation-dependent trend is revealed. As the axial orientation shifts from low-index (⟨100⟩, ⟨110⟩, ⟨111⟩) toward a random high-index direction, the pillars progressively adopt more spheroidal shapes and exhibit reduced ability to retain their original height. The differences can be attributed to variations in surface-energy anisotropy and adatom generation across different axial orientations. Our findings offer new insights into how crystallographic orientation governs thermal morphological evolution in one-dimensional nanostructures. They further suggest axial orientation control, without altering composition or surface chemistry, as a viable strategy for designing thermally reliable nanoscale systems.

Figure 1 reveals the morphologies of single-crystalline α-Fe pillars oriented along the ⟨100⟩, ⟨110⟩ and ⟨111⟩ directions after annealing at ~600 °C. All three pillars exhibited pronounced orientation-dependent evolution in both height and shape, as compared with the original profiles marked with white dotted lines in Figures 1a–c. The pillar with ⟨100⟩ axial direction (hereafter referred to as the ⟨100⟩ pillar, and the other pillars are named accordingly) remained relatively stable, undergoing a negligible height reduction of ~20 nm (by ~3% of initial height) after holding at 600 °C for ~10 min. In contrast, the ⟨110⟩ and ⟨111⟩ pillars shortened by ~280 nm (~31%) and ~390 nm (~43%), respectively, after holding for ~5 min. This dimensional change was accompanied by varying degrees of spheroidization, which were quantified using the projected spheroidization degree, D_{sph}, defined in Note S1 and Table S1. The ⟨100⟩ pillar transformed into a well-defined octagonal prism with a flat {100} top facet ($D_{sph} \approx 0.09$). For the ⟨110⟩ pillar, by contrast, despite the top view becoming octagonal, the

https://doi.org/10.1021/acs.nanolett.6c01885
Nano Lett. 2026, 26, 8551−8558

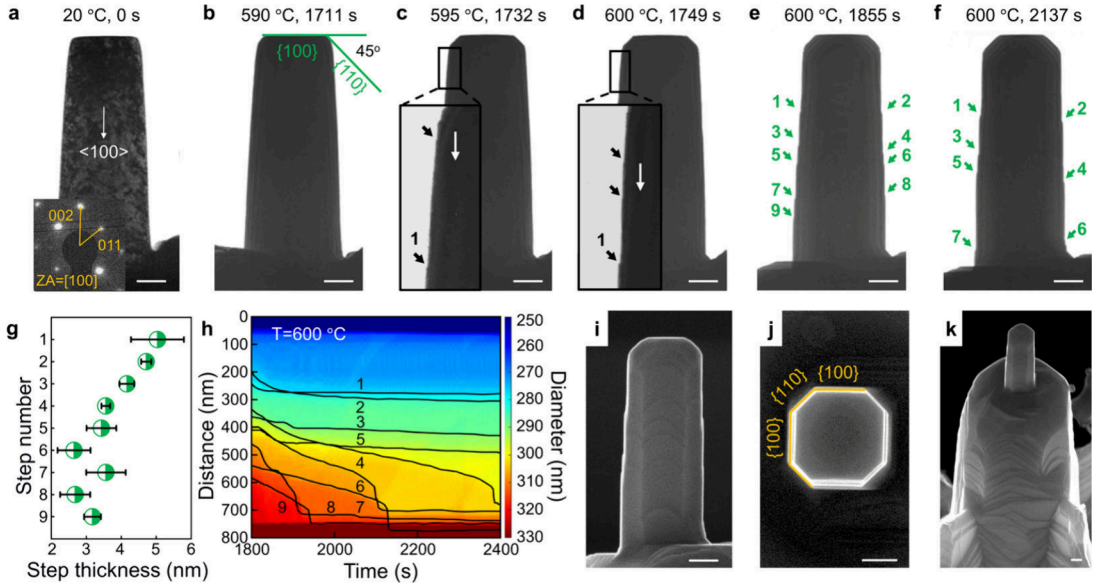

Figure 2. Morphological evolution of the ⟨100⟩ α-Fe pillar. (a) The bright-field TEM image of a typical pillar with a diameter of ∼300 nm before heating. (b) The shape transformation starts from the top-corner region of the pillar. (c,d) Steps are generated on the side surfaces and move downward, indicated by the black arrows, leading to the formation of a multiatomic-layer step. (e,f) Nine multiatomic-layer steps, indicated by the green arrows, emerge on the side of the pillar and move to the matrix (see Movie S1). (g) The average thicknesses of the nine multiatomic-layer steps. (h) The distance between the nine steps and the top of the pillar versus time. (i, j) SEM images of the pillar after heating viewed from the side and top, respectively. The pillar transforms into an octagonal prism with obvious steps on the side. (k) SEM image with a larger field of view. The same phenomena are also observed on the matrix. The timestamps above the TEM snapshots denote the total elapsed time from the start of heating at room temperature. All scale bars: 100 nm.

top {110} facet almost disappeared, resulting in a pyramid-like shape ($D_{sph} \approx 0.40$). The facets with recognizable indices on these two pillars are indicated in Figures 1g,h. For the ⟨111⟩ pillar, it underwent a more pronounced spheroidization process, with its top region approaching a hemispheroidal shape ($D_{sph} \approx 0.61$) and no facets being discernible. All these morphological features were also reproduced under a beam-off condition (Figure S2), thus verifying the reproducibility of the results and ruling out the influence of electron-beam irradiation on this morphological evolution. The experimental conditions and the corresponding morphological changes before and after heating for all representative pillars are summarized in Table S2.

Such processes are anisotropic and governed by surface-energy minimization. Previous studies have shown that whether a thermally evolving surface preserves well-defined facets or instead undergoes spheroidization depends on how strongly the surface energy varies with crystallographic orientation. This orientation dependence can be represented by the surface-energy polar plot (γ-plot), in which deep minima (cusps) correspond to the lowest-energy surface orientations and indicate a steep angular variation in surface energy, thereby reflecting strong anisotropy. Such pronounced cusps stabilize energetically favored orientations, promote the development of missing orientations in the equilibrium shape, and cause flat facets to replace smooth segments. As the cusps smooth out, the anisotropy weakens, reducing the thermodynamic driving force for faceting and making the equilibrium shape increasingly spheroidal.[24,37−39] Geometrically, sidewall reshaping is constrained to facets whose surface normal vectors are perpendicular to the pillar axis. Consequently, varying the axial orientation selects a different subset of accessible facets and thereby changes the relevant cross-section of the 3D γ-plot, whose angular variation constitutes the effective surface-energy anisotropy governing sidewall reshaping. We therefore attribute the orientation-dependent spheroidization to differences in effective surface-energy anisotropy, as illustrated in Figures 1g−i. For the ⟨100⟩ pillar, the sidewalls readily reconstruct into {110} and {100} facets, which correspond to deep cusps in the γ-plot of α-Fe (Figure 1g). This sharp energetic landscape produces pronounced effective anisotropy, thereby stabilizing the facets and suppressing the thermodynamic driving force for spheroidization. The ⟨110⟩ pillar possesses sidewalls composed of {100}, {110} and {111} facets. The presence of the {111} facets, which have a higher surface energy (Table S3), bridges the energy gaps between the major γ-plot cusps (Figure 1h), smoothing the energetic landscape. This reduction in effective anisotropy promotes partial spheroidization, although faceting remains. Furthermore, for the ⟨111⟩ pillar, geometric constraints introduce a larger fraction of high-index sidewall orientations (e.g., {211} and {321}), where surface energies vary weakly. This flattened energy landscape (Figure 1i) reduces effective anisotropy and favors full spheroidization. Similar morphological changes in smaller nanoparticles (typically <20 nm in size) were attributed to surface premelting.[40−42] However, such a mechanism is unlikely here. For pillars with a diameter of ∼300 nm, the premelting temperature is predicted to be close to the T_m,[41,42] well above the present annealing temperature of 0.48 T_m.

While surface-energy anisotropy accounts for the orientation-dependent extent of spheroidization, the remarkably different shortening rates indicate distinct mass-transport kinetics. In our *in situ* TEM recordings (Movies S1 and S2), surface steps are visible on both the ⟨100⟩ and ⟨110⟩ nanopillars and their surrounding matrix. According to the Burton-Cabrera-Frank theory,[43] such surface steps can act as efficient sinks and sources for diffusing adatoms. They also modify the local chemical potential via the Gibbs−Thomson effect and strongly affect diffusion kinetics.[44] Quantifying step dynamics, therefore,

https://doi.org/10.1021/acs.nanolett.6c01885
Nano Lett. 2026, 26, 8551−8558

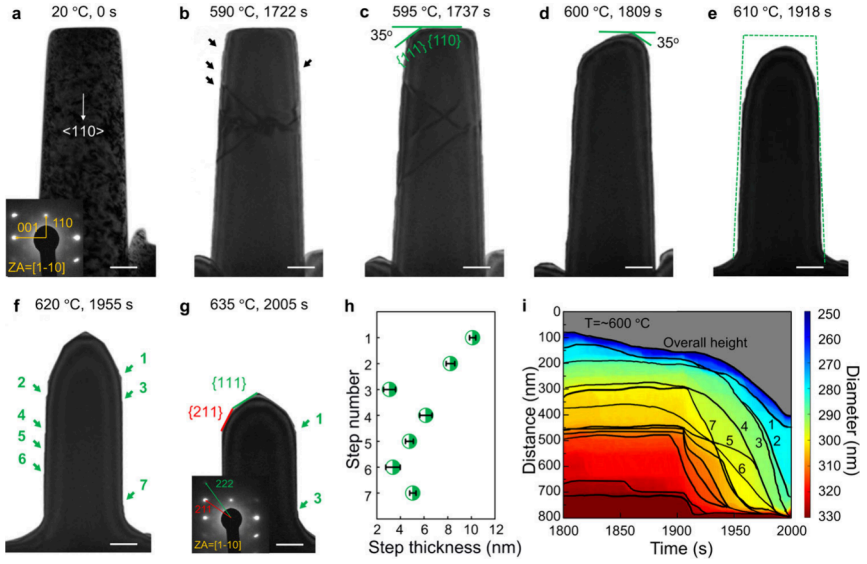

Figure 3. Morphological evolution of the ⟨110⟩ α-Fe pillar. (a) The bright-field TEM image of a typical pillar with a diameter of ∼ 300 nm before heating. (b) Steps are generated on the side surfaces indicated by the black arrows. (c−e) The shape transformation starts from the top-corner region of the pillar. The green dotted lines in (e) represent the original profile. (f,g) Seven multiatomic-layer steps form. The height of the pillar decreases in this period (see Movie S2). (h) The average thicknesses of the seven multiatomic-layer steps. (i) The distance between the seven steps and the original top position of the pillar versus time. The timestamps above the TEM snapshots denote the total elapsed time from the start of heating at room temperature. All scale bars: 100 nm.

provides a direct probe of the kinetic origin of the orientation dependence. The analyses are summarized in Figure 2 (Movie S1) for the ⟨100⟩ pillar and in Figure 3 (Movie S2) for the ⟨110⟩ pillar. For all pillars, before heating to the observation temperature of ∼600 °C, the high-density preexisting FIB-induced dislocations were annealed out, leaving the pillars essentially defect-free in the interior (Figures 2a,b and Figures 3a,b). Thus, the subsequent morphological evolution was dominated by surface diffusion. For the ⟨100⟩ pillar, upon further heating to 600 °C, the cylindrical pillar gradually transformed into an octagonal prism bounded by {100} and {110} side facets, with the top corners of the pillar reconstructed to form new {110} facets. At these side facets, steps emerged (black arrows in Figures 2c,d), migrated downward (white arrow) and coalesced into several distinct steps by 600 °C (green arrows in Figure 2e). Their measured thicknesses ranged from ∼2.8 to 5.0 nm (Figure 2g). The temporal evolution of the step distances from the pillar top is plotted in Figure 2h, with numbering corresponding to Figures 2e,f. Steps at the lower positions continued to migrate downward, while those near the top showed negligible motion. Meanwhile, the overall pillar height remained nearly constant during holding at 600 °C, as shown in Figure S3.

The evolution of the ⟨110⟩ pillar at the early stage resembled that of the ⟨100⟩ pillar, in terms of dislocation annihilation and initial step accumulation. After dislocation removal, however, the top {110} facet was progressively consumed by newly formed {111} facets. The tip then adopted a transiently spheroidal shape, temporarily losing well-defined facets before stabilizing into a pyramid-like morphology bounded by {111} and {211} facets (Figures 3c−g). This behavior indicates a greater tendency toward spheroidization than in the ⟨100⟩ pillar, consistent with the reduced anisotropy effect discussed above. In addition, the ⟨110⟩ pillar revealed a much faster height reduction, about 30 times that of the ⟨100⟩ pillar (Figure S3). If held at this temperature for longer periods, the pillar fully retracted into the matrix (Figure S4). Surface-step kinetics were also remarkably different. Both the average step thickness and the downward migration rate on the <110> pillar were notably larger than those on the ⟨100⟩ pillar (Figures 3h,i).

Before discussing the relationship between step motion and pillar shortening, it is essential to consider how these steps form. Although dislocation annihilation may generate early surface perturbations, it cannot explain why pronounced steps appeared only in the ⟨100⟩ and ⟨110⟩ pillars but not in the ⟨111⟩ pillar. We therefore attribute the primary origin of these steps to the ∼3.5° taper angle introduced during FIB fabrication. This taper renders the sidewall facets vicinal, causing them to decompose into low-energy singular terraces separated by steps.[24,45] At 590 °C, surface diffusion is enhanced. A chemical potential gradient between the highly curved tip and the flat matrix drives adatom diffusion away from the tip.[44] During adatom migration toward the matrix, steps act as barriers, impeding the upward interlayer transport relative to the rapid intralayer diffusion on terraces. Thus, the retreat velocity of each step becomes highly sensitive to the width of the terrace below.[46−48] Minor fluctuations in terrace width are therefore amplified, causing adjacent steps to develop different retreat velocities. This leads to step bunching and the formation of the multiatomic-layer steps,[49,50] as observed experimentally. Such steps increase the density of active surface sites and modify surface roughness, with potential implications for the optical, mechanical, catalytic, and corrosion-resistant properties of the nanostructures.[51−54] In contrast, for the ⟨111⟩ pillar, early spheroidization prevents the sidewall from decomposing into stable low-energy terraces, and steps therefore do not form.

Next, we estimate the number of atoms transported into the matrix by step motion on the ⟨100⟩ and ⟨110⟩ pillars (see Note S2 and Table S4 for details). The ⟨110⟩ pillar shows an average transport rate of 1.3×10^6 atoms s^{-1}, nearly 30 times higher than the rate of 4.2×10^4 atoms s^{-1} measured on the ⟨100⟩ pillar. This difference matches the observed disparity in pillar-shortening

https://doi.org/10.1021/acs.nanolett.6c01885
Nano Lett. 2026, 26, 8551−8558

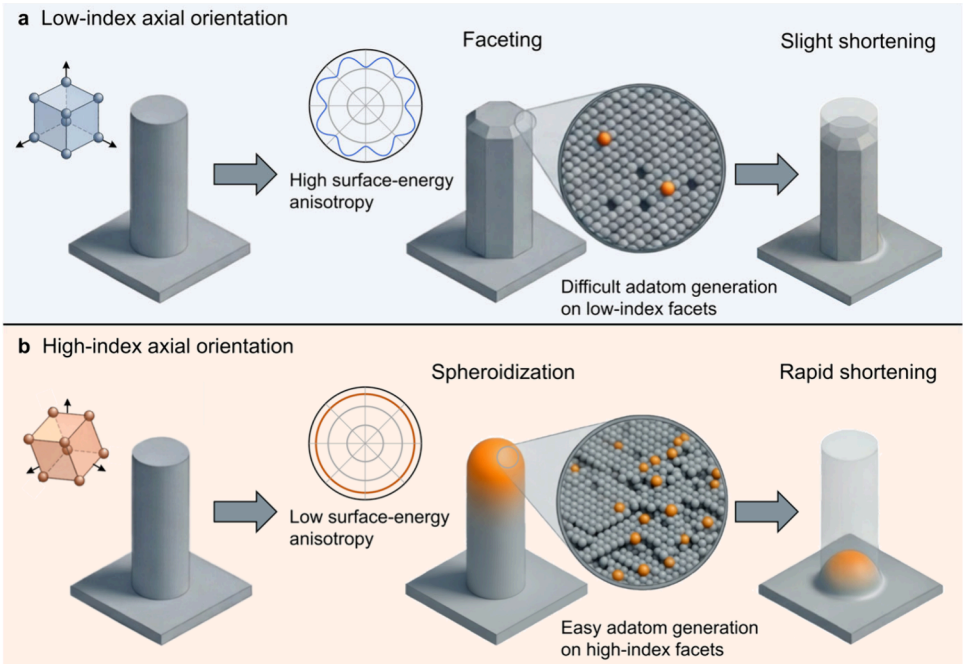

Figure 4. Illustration of the mechanism governing the orientation-dependent thermal morphological evolution of α-Fe nanopillars. As the axial orientation shifts from low-index (a) to high-index (b), the decrease in effective surface energy anisotropy facilitates spheroidization. Simultaneously, the increased exposure of high-index facets and edges boosts adatom formation (as indicated by the orange balls), significantly accelerating pillar shortening.

rates, confirming that the overall height reduction is predominantly governed by the surface-diffusion-mediated transport of atoms from the tip into the matrix.

Surface-diffusion-mediated mass transport from the tip to the matrix involves two steps: formation of α-Fe adatoms through bond rupture, and their subsequent migration across the surface. Within the terrace-step-kink framework, high-index facets can be decomposed into closely spaced terraces separated by monatomic steps and kinks. This configuration creates a high density of low-coordination surface sites. Atoms at such sites require fewer bonds to break for detachment, lowering the adatom formation energy compared with densely packed, low-index facets.[55−57] Molecular dynamics simulation of α-Fe supports this trend: formation energies of adatoms on {110}, {100}, and {111} facets are 1.03, 0.58, and 0.09 eV, respectively, showing a decreasing trend. In contrast, the corresponding migration energies are 0.24, 0.84, and 0.97 eV, showing an increasing trend.[26] These results reveal a kinetic asymmetry. High-index surfaces facilitate adatom generation, but contain dense networks of steps and kinks that introduce line tension and trapping-detrapping energy barriers. This creates a corrugated potential energy landscape with deep trapping sites that impede lateral adatom migration.[27,44,58] In contrast, low-index facets possess wider terraces and fewer steps. They therefore impose higher adatom formation energy but provide smoother migration pathways. Consequently, increasing the facet index promotes adatom generation while suppressing migration, creating a competition between detachment kinetics and surface migration.

Thus, compared with the ⟨100⟩ pillar fully bounded by low-index {100} and {110} facets on its sidewalls and top corners, the ⟨110⟩ pillar, bounded by higher-index facets ({111} and {211}), should favor easier adatom generation yet more sluggish adatom migration. The much faster shortening observed on the ⟨110⟩ pillar, therefore, implies that the availability of adatoms outweighs the penalty of their slower migration. This result suggests that adatom formation, rather than their migration, is the rate-limiting step in surface diffusion, and thus controls the overall shortening rate of the nanopillars. An Arrhenius-type estimate based on these values further shows that the higher adatom formation energy on low-index facets can outweigh their lower migration barriers. At 600 °C, the estimated effective atomic transport rates on {111} and {110} are approximately 120 and 7 times higher than that on {100}, respectively (Note S3). This mechanism is further supported by the cessation of mass loss at the {110} corner facets on the ⟨100⟩ pillar during the initial stage. Because the pillar geometry and the facet indices remain essentially unchanged before and after this cessation, the migration barrier should also remain constant. The halted mass transport, therefore, points to an insufficient supply of adatoms rather than limited mobility, further supporting that adatom generation governs overall surface diffusion kinetics.

Integrating these findings, we propose a unified mechanism to elucidate how axial orientation governs the thermal morphological evolution of the nanopillars, as illustrated in Figure 4. An increase in the axial index reduces effective surface-energy anisotropy, shifting the evolution pathway away from stabilizing low-energy facets toward spheroidization as the primary route to minimize the total surface energy. As spheroidization becomes more pronounced, the area fraction of high-index facets and curved edges increases, thereby facilitating adatom formation. This enhanced adatom production accelerates mass transport from the tip to the matrix, resulting in faster pillar shortening. Within this framework, the distinct behaviors of the ⟨100⟩, ⟨110⟩, and ⟨111⟩ α-Fe pillars can be rationalized. For the ⟨100⟩ pillar, the ready exposure of low-energy {100} and {110} facets preserves a strong effective anisotropy and limits adatom supply, thereby stabilizing both its faceted morphology and overall height. By contrast, the geometric constraints imposed by the ⟨110⟩ and ⟨111⟩ axial orientations favor the exposure of more

https://doi.org/10.1021/acs.nanolett.6c01885
Nano Lett. 2026, 26, 8551−8558

high-index facets and edges, which weaken the effective anisotropy, promote spheroidization, and accelerate axial shortening through enhanced adatom generation and sustained mass transport.

To further validate this mechanism, we investigated the thermal morphological evolution of a nanopillar with a random high-index axial orientation, close to ⟨413⟩, as presented in Figure 5a. According to the proposed mechanism, this pillar

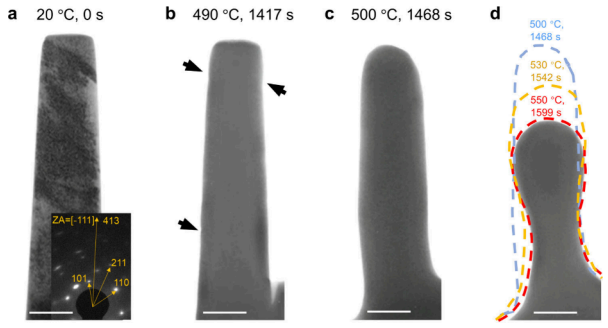

Figure 5. Morphological evolution of the ⟨413⟩ α-Fe pillar. (a) The bright-field TEM image of the pillar before heating. (b) The visible dislocations are annihilated, and a few steps, as indicated by black arrows, appear on the surfaces below 490 °C. (c) The pillar starts to spheroidize at 500 °C. (d) With increasing temperature, the pillar gradually shrinks toward the matrix and evolves into a highly spheroidized shape (see Movie S3). The timestamps above the TEM snapshots denote the total elapsed time from the start of heating at room temperature. All scale bars: 200 nm.

should exhibit greater spheroidization due to the reduced surface-energy anisotropy, together with a faster height reduction driven by the rapid adatom generation on the high-index facets. Our observations are consistent with this prediction (Movie S3). As shown in Figures 5b,c, surface step motion was activated at 490 °C after the pillar became dislocation-free, and the tip began to spheroidize at 500 °C. During subsequent heating from 500 to 550 °C, the pillar progressively evolved into a highly spheroidized morphology ($D_{sph} \approx 0.67$), as depicted by the colored dotted contours in Figure 5d. Notably, the onset temperatures for both spheroidization and height reduction (~500 °C) in the ⟨413⟩ pillar are significantly lower than 600 °C. Furthermore, the shortening rate is approximately twice that measured for the ⟨110⟩ pillar (Figure S3). The observed necking may be partly associated with Rayleigh instability. The larger aspect ratio of this pillar (~4.7, being ~1.7 times that of the ⟨110⟩ pillar) allows perturbation wavelengths exceeding the critical circumference, thereby triggering the instability.[59] This may amplify the late-stage necking and apparent shortening. However, because surface-step activation, spheroidization, and axial shortening already occur at 490−510 °C before pronounced necking develops, the behavior of the ⟨413⟩ pillar still supports enhanced spheroidization tendency and elevated adatom generation associated with the high-index axial orientation. The effects of the surface oxide layer and sample dimensions are evaluated and found not to affect the reliability of the observed trend (see Notes S4, S5 and Figures S5-S7).

In summary, we systematically investigated the thermal morphological response in single-crystalline α-Fe nanopillars with different axial orientations. As the axis changes from ⟨100⟩ to ⟨110⟩, ⟨111⟩, and ⟨413⟩ orientation, the nanopillars exhibit stronger spheroidization and faster axial shortening. This divergence arises from a coupled thermodynamic-kinetic effect. Increasing the axial index reduces the effective surface-energy anisotropy, shifting the dominant energy minimization pathway from facet-preserving reconstruction toward global surface-area reduction. At the same time, the resulting increased exposure of high-index facets and step edges enhances adatom formation. Our results strongly indicate that this enhanced adatom availability, rather than adatom migration alone, sustains rapid surface mass transport from the tip into the matrix and accelerates pillar shortening. Accordingly, low-index facets, which are naturally associated with higher adatom formation energy, provide greater resistance against high-temperature reshaping and shortening.

It is worth noting that face-centered cubic and hexagonal close-packed metals may possess stable facets and diffusion barriers that differ from those of body-centered cubic α-Fe. Thus, the terminology of "low-index" and "high-index" is not directly transferable across crystal structures. Nevertheless, the underlying determining factors remain consistent: whether a given axial orientation enables low-energy faceting with pronounced surface-energy cusps, and how it affects adatom kinetics. Therefore, by incorporating material-specific surface-energy anisotropy and surface-diffusion kinetics, the thermodynamic-kinetic framework provides a general basis for assessing orientation-dependent evolution pathways in metallic nanowires and nanopillars.

From a practical perspective, this novel insight is directly relevant to nanoscale devices, such as nanoelectronic interconnects, transparent nanowire electrodes, and nanocatalysts, where thermally activated surface diffusion often drives shape instability and performance degradation. Adsorbates or reactive gases such as O_2, H_2O, H_2 and CO_2 in realistic atmospheres can modify facet-dependent surface energies, shift the cusps in the surface-energy polar plot, and change the preferred facets and evolution pathway. Thus, the environment-specific changes in surface-energy anisotropy and adatom kinetics should also be incorporated when evaluating atmosphere-dependent morphological stability. Controlling axial orientation, therefore, offers a simple strategy to tailor thermal evolution pathways and improve structural resilience, without changing composition or intentionally modifying surface chemistry.

■ ASSOCIATED CONTENT

Supporting Information

The Supporting Information is available free of charge at https://pubs.acs.org/doi/10.1021/acs.nanolett.6c01885.

Experimental methods and setup, electron-beam and oxide-layer effects, time-dependent pillar-length evolution, effects of prolonged annealing, quantification of projected spheroidization degree, summary of morphological changes of all nanopillars and Fe surface energies, step-kinetics calculation details, Arrhenius estimate of adatom generation−migration competition and assessment of the size effect (PDF)

In situ TEM movie showing the thermal morphological evolution of the ⟨100⟩ α-Fe pillar during heating to and holding near ~600 °C (MP4)

In situ TEM movie showing the thermal morphological evolution of the ⟨110⟩ α-Fe pillar during heating to and holding near ~600 °C (MP4)

https://doi.org/10.1021/acs.nanolett.6c01885
Nano Lett. 2026, 26, 8551−8558

In situ TEM movie showing the thermal morphological evolution of the ⟨413⟩ α-Fe pillar during heating from ~480 to ~550 °C (MP4)

AUTHOR INFORMATION

Corresponding Author

Degang Xie − *Center for Advancing Materials Performance from the Nanoscale (CAMP-Nano), State Key Laboratory for Mechanical Behavior of Materials, Xi'an Jiaotong University, Xi'an 710049, People's Republic of China;* orcid.org/0009-0008-2082-226X; Email: dg_xie@xjtu.edu.cn

Authors

Longqi Bai − *Center for Advancing Materials Performance from the Nanoscale (CAMP-Nano), State Key Laboratory for Mechanical Behavior of Materials, Xi'an Jiaotong University, Xi'an 710049, People's Republic of China; Max Planck Institute for Sustainable Materials, Düsseldorf 40237, Germany*

Longchao Huang − *Center for Advancing Materials Performance from the Nanoscale (CAMP-Nano), State Key Laboratory for Mechanical Behavior of Materials, Xi'an Jiaotong University, Xi'an 710049, People's Republic of China; Western Superconducting Technologies Co Ltd, Xi'an 710018, People's Republic of China;* orcid.org/0000-0001-7832-7271

Yan Ma − *Department of Materials Science & Engineering, Delft University of Technology, 2628 CD Delft, The Netherlands*

Zhiwei Shan − *Center for Advancing Materials Performance from the Nanoscale (CAMP-Nano), State Key Laboratory for Mechanical Behavior of Materials, Xi'an Jiaotong University, Xi'an 710049, People's Republic of China;* orcid.org/0000-0002-4533-0869

Complete contact information is available at: https://pubs.acs.org/10.1021/acs.nanolett.6c01885

Author Contributions

L.B., L.H., and Y.M. contributed equally to this work. D.X. and Z.S. conceived and supervised the project. L.H. and L.B. carried out the experimental works. L.B., D.X., Y.M., and L.H. conducted the data analysis and presentation. L.B., Y.M., and D.X. wrote the paper. All the authors contributed to the discussions.

Notes

The authors declare no competing financial interest.

ACKNOWLEDGMENTS

The authors acknowledge the support of the National Natural Science Foundation of China (Grant No. 52522103 and Grant No. 52371122), and the Shaanxi Province Foundation for Distinguished Young Scholars (Grant No. 2024JC-JCQN-47). L.B. acknowledges the financial support from the China Scholarship Council (No. 202306280003). The authors would like to thank Dr. Chengguang Wu for his assistance with the experiments and for the helpful discussions.

REFERENCES

(1) Chen, J.; Wiley, B. J.; Xia, Y. One-Dimensional Nanostructures of Metals: Large-Scale Synthesis and Some Potential Applications. *Langmuir* **2007**, *23* (8), 4120−4129.

(2) Xie, D.-G.; Nie, Z.-Y.; Shinzato, S.; Yang, Y.-Q.; Liu, F.-X.; Ogata, S.; Li, J.; Ma, E.; Shan, Z.-W. Controlled Growth of Single-Crystalline Metal Nanowires via Thermomigration across a Nanoscale Junction. *Nat. Commun.* **2019**, *10* (1), 4478.

(3) Nawaz, M. H.; Kumar, A.; Chuang, F.-C.; Ponnusamy, V. K.; Pham, P. V. The World of Metal Nanowires: Recent Advances in Syntheses, Electronic Applications, and Engineering Challenges. *Mater. Today* **2026**, *92*, 606−669.

(4) Shah, K. W.; Xiong, T. Multifunctional Metallic Nanowires in Advanced Building Applications. *Materials* **2019**, *12* (11), 1731.

(5) Xia, Y.; Yang, P.; Sun, Y.; Wu, Y.; Mayers, B.; Gates, B.; Yin, Y.; Kim, F.; Yan, H. One-Dimensional Nanostructures: Synthesis, Characterization, and Applications. *Adv. Mater.* **2003**, *15* (5), 353−389.

(6) Elmekawy, A. H. A.; Iashina, E.; Dubitskiy, I. S.; Sotnichuk, S.; Bozhev, I. V.; Kozlov, D.; Napolskii, K. S.; Menzel, D.; Mistonov, A. A. Magnetic Properties of Ordered Arrays of Iron Nanowires: The Impact of the Length. *J. Magn. Magn. Mater.* **2021**, *532*, No. 167951.

(7) Ou, M. N.; Yang, T. J.; Chen, Y. Y. Anisotropic Magnetism and Magnetoresistance in Iron Nanowire Arrays. *Chin. J. Phys.* **2009**, *47* (6), 847−852.

(8) Ren, Y.; Liu, Q. F.; Li, S. L.; Wang, J. B.; Han, X. H. The Effect of Structure on Magnetic Properties of Co Nanowire Arrays. *J. Magn. Magn. Mater.* **2009**, *321* (3), 226−230.

(9) Zhao, P.; Cheng, Y.; Li, L.; Jia, S.; Guan, X.; Huang, T.; Li, L.; Zheng, H.; Wang, J. Revealing the Structure/Property Relationships of Semiconductor Nanomaterials via Transmission Electron Microscopy. *Adv. Funct. Mater.* **2025**, *35* (1), No. 2408935.

(10) Sondheimer, E. H. The Mean Free Path of Electrons in Metals. *Adv. Phys.* **2001**, *50* (6), 499−537.

(11) Zhu, Y.; Dou, X.; Huang, X.; Li, L.; Li, G. Thermal Properties of Bi Nanowire Arrays with Different Orientations and Diameters. *J. Phys. Chem. B* **2006**, *110* (51), 26189−26193.

(12) Stewart, I. E.; Kim, M. J.; Wiley, B. J. Effect of Morphology on the Electrical Resistivity of Silver Nanostructure Films. *ACS Appl. Mater. Interfaces* **2017**, *9* (2), 1870−1876.

(13) Wang, L.; Zhang, Z.; Han, X. In Situ Experimental Mechanics of Nanomaterials at the Atomic Scale. *NPG Asia Mater.* **2013**, *5* (2), No. e40.

(14) Zhang, S. B. Microstructure- and Surface Orientation-Dependent Mechanical Behaviors of Ag Nanowires under Bending. *Comput. Mater. Sci.* **2014**, *95*, 53−62.

(15) Sainath, G.; Choudhary, B. K. Orientation-Dependent Deformation Behaviour of BCC Iron Nanowires. *Comput. Mater. Sci.* **2016**, *111*, 406−415.

(16) Yang, Y.; Wang, S. Y.; Xiang, B.; Yin, S.; Pekin, T. C.; Li, X.; Zhang, R.; Yano, K.; Hwang, D.; Asta, M.; Grigoropoulos, C.; Allen, F. I.; Minor, A. M. Evaluating the Effects of Pillar Shape and Gallium Ion Beam Damage on the Mechanical Properties of Single Crystal Aluminum Nanopillars. *J. Mater. Res.* **2021**, *36* (12), 2515−2528.

(17) Xie, S.; Choi, S.-I.; Xia, X.; Xia, Y. Catalysis on Faceted Noble-Metal Nanocrystals: Both Shape and Size Matter. *Curr. Opin. Chem. Eng.* **2013**, *2* (2), 142−150.

(18) Zhou, K.; Li, Y. Catalysis Based on Nanocrystals with Well-Defined Facets. *Angew. Chem., Int. Ed.* **2012**, *51* (3), 602−613.

(19) Lu, Y.; Chen, Y.; Zeng, Y.; Zhang, Y.; Kong, D.; Li, X.; Zhu, T.; Li, X.; Mao, S.; Zhang, Z.; Wang, L.; Han, X. Nanoscale Ductile Fracture and Associated Atomistic Mechanisms in a Body-Centered Cubic Refractory Metal. *Nat. Commun.* **2023**, *14* (1), 5540.

(20) Cho, H.; Shin, J. W.; Ryoo, R. Atomic Scale Mechanisms Underlying Thermal Reshaping of Anisotropic Gold Nanocrystals Revealed by In Situ Electron Microscopy. *J. Phys. Chem. C* **2020**, *124* (23), 12855−12863.

(21) Petrova, H.; Perez Juste, J.; Pastoriza-Santos, I.; Hartland, G. V.; Liz-Marzán, L. M.; Mulvaney, P. On the Temperature Stability of Gold Nanorods: Comparison between Thermal and Ultrafast Laser-Induced Heating. *Phys. Chem. Chem. Phys.* **2006**, *8* (7), 814−821.

(22) Chi, M.; Wang, C.; Lei, Y.; Wang, G.; Li, D.; More, K. L.; Lupini, A.; Allard, L. F.; Markovic, N. M.; Stamenkovic, V. R. Surface Faceting and Elemental Diffusion Behaviour at Atomic Scale for Alloy

Nanoparticles during In Situ Annealing. *Nat. Commun.* **2015**, *6* (1), 8925.
(23) Wulff, G. XXV. Zur Frage der Geschwindigkeit des Wachsthums und der Auflösung der Krystallflächen. *Z. Kristallogr. - Cryst. Mater.* **1901**, *34* (1−6), 449−530.
(24) Herring, C. Some Theorems on the Free Energies of Crystal Surfaces. *Phys. Rev.* **1951**, *82* (1), 87−93.
(25) Elliott, J. A. W. Gibbsian Surface Thermodynamics. *J. Phys. Chem. B* **2020**, *124* (48), 10859−10878.
(26) Yin, X.; Wang, X. Kinetics-Driven Crystal Facets Evolution at the Tip of Nanowires: A New Implementation of the Ostwald-Lussac Law. *Nano Lett.* **2016**, *16* (11), 7078−7084.
(27) Wang, C.; Qin, Z.; Zhang, Y.; Sun, Q.; Jia, Y. A Molecular Dynamics Simulation of Self-Diffusion on Fe Surfaces. *Appl. Surf. Sci.* **2012**, *258* (10), 4294−4300.
(28) Wang, Y.; Teitel, S.; Dellago, C. Surface-Driven Bulk Reorganization of Gold Nanorods. *Nano Lett.* **2005**, *5* (11), 2174−2178.
(29) Wang, Y.; Teitel, S.; Dellago, C. Effect of Surface Structure on Shape Transformations of Gold Nanorods. *J. Comput. Theor. Nanosci.* **2007**, *4* (2), 282−290.
(30) Pan, L. S.; Zhang, Y. W.; Lee, H. P. Effects of Crystal Orientations of the Facets on the Structural Stability of Metallic Ni Nanorods. *J. Nanopart. Res.* **2010**, *12* (3), 795−800.
(31) Wen, Y.-H.; Zhang, Y.; Zheng, J.-C.; Zhu, Z.-Z.; Sun, S.-G. Orientation-Dependent Structural Transition and Melting of Au Nanowires. *J. Phys. Chem. C* **2009**, *113* (48), 20611−20617.
(32) Wirth, C. T.; Bayer, B. C.; Gamalski, A. D.; Esconjauregui, S.; Weatherup, R. S.; Ducati, C.; Baehtz, C.; Robertson, J.; Hofmann, S. The Phase of Iron Catalyst Nanoparticles during Carbon Nanotube Growth. *Chem. Mater.* **2012**, *24* (24), 4633−4640.
(33) Winterbottom, W. L. Equilibrium Shape of a Small Particle in Contact with a Foreign Substrate. *Acta Metall.* **1967**, *15* (2), 303−310.
(34) Damerchi, E.; Oras, S.; Butanovs, E.; Liivlaid, A.; Antsov, M.; Polyakov, B.; Trausa, A.; Zadin, V.; Kyritsakis, A.; Vidal, L.; Mougin, K.; Pikker, S.; Vlassov, S. Heat-Induced Morphological Changes in Silver Nanowires Deposited on a Patterned Silicon Substrate. *Beilstein J. Nanotechnol.* **2024**, *15*, 435−446.
(35) Karim, S.; Toimil-Molares, M. E.; Balogh, A. G.; Ensinger, W.; Cornelius, T. W.; Khan, E. U.; Neumann, R. Morphological Evolution of Au Nanowires Controlled by Rayleigh Instability. *Nanotechnology* **2006**, *17* (24), 5954−5959.
(36) Li, H.; Biser, J. M.; Perkins, J. T.; Dutta, S.; Vinci, R. P.; Chan, H. M. Thermal Stability of Cu Nanowires on a Sapphire Substrate. *J. Appl. Phys.* **2008**, *103* (2), No. 024315.
(37) Gurski, K. F.; McFadden, G. B. The Effect of Anisotropic Surface Energy on the Rayleigh Instability. *Proc. R. Soc. London, Ser. A* **2003**, *459* (2038), 2575−2598.
(38) Einstein, T. L. Equilibrium Shape of Crystals. In *Handbook of Crystal Growth*, 2nd ed.; Nishinaga, T., Ed.; Elsevier: 2015; Vol. *IA*, pp 215−264.
(39) Bonzel, H. P. 3D Equilibrium Crystal Shapes in the New Light of STM and AFM. *Phys. Rep.* **2003**, *385* (1−2), 1−67.
(40) Wang, K.; Wu, H.; Ge, M.; Xi, W.; Luo, J. Exponential Surface Melting of Cu Nanoparticles Observed by In Situ TEM. *Mater. Charact.* **2018**, *145*, 246−249.
(41) Liu, X.; Wen, X.; Hoffmann, R. Surface Activation of Transition Metal Nanoparticles for Heterogeneous Catalysis: What We Can Learn from Molecular Dynamics. *ACS Catal.* **2018**, *8* (4), 3365−3375.
(42) Wu, Y.-N.; Huang, R.; Zeng, X.-M.; Wen, Y.-H. Octadecahedral and Dodecahedral Iron Nanoparticles: An Atomistic Simulation on Stability and Shape Evolutions. *Phys. Lett. A* **2016**, *380* (5−6), 739−744.
(43) Burton, W. K.; Cabrera, N.; Frank, F. C. The Growth of Crystals and the Equilibrium Structure of Their Surfaces. *Philos. Trans. R. Soc. London, Ser. A* **1951**, *243* (866), 299−358.
(44) Jeong, H.-C.; Williams, E. D. Steps on Surfaces: Experiment and Theory. *Surf. Sci. Rep.* **1999**, *34* (6−8), 171−294.
(45) Williams, E. D.; Bartelt, N. C. Thermodynamics of Surface Morphology. *Science* **1991**, *251* (4992), 393−400.
(46) Frisch, T.; Verga, A. Kinetic Step Bunching Instability during Surface Growth. *Phys. Rev. Lett.* **2005**, *94* (22), No. 226102.
(47) Schwoebel, R. L.; Shipsey, E. J. Step Motion on Crystal Surfaces. *J. Appl. Phys.* **1966**, *37* (10), 3682−3686.
(48) Ehrlich, G.; Hudda, F. G. Atomic View of Surface Self-Diffusion: Tungsten on Tungsten. *J. Chem. Phys.* **1966**, *44* (3), 1039−1049.
(49) Hamouda, A. B. H.; Pimpinelli, A.; Einstein, T. L. Narrowing of Terrace-Width Distributions during Growth on Vicinal Surfaces. *EPL* **2009**, *88* (2), 26005.
(50) Schwoebel, R. L. Step Motion on Crystal Surfaces. II. *J. Appl. Phys.* **1969**, *40* (2), 614−618.
(51) Baumberger, F.; Herrmann, Th; Kara, A.; Stolbov, S.; Esser, N.; Rahman, T. S.; Osterwalder, J.; Richter, W.; Greber, T. Optical Recognition of Atomic Steps on Surfaces. *Phys. Rev. Lett.* **2003**, *90* (17), No. 177402.
(52) Xu, L.; Papanikolaou, K. G.; Lechner, B. A. J.; Je, L.; Somorjai, G. A.; Salmeron, M.; Mavrikakis, M. Formation of Active Sites on Transition Metals through Reaction-Driven Migration of Surface Atoms. *Science* **2023**, *380* (6640), 70−76.
(53) Kim, S. J.; Kim, Y. I.; Lamichhane, B.; Kim, Y.-H.; Lee, Y.; Cho, C. R.; Cheon, M.; Kim, J. C.; Jeong, H. Y.; Ha, T.; Kim, J.; Lee, Y. H.; Kim, S.-G.; Kim, Y.-M.; Jeong, S.-Y. Flat-Surface-Assisted and Self-Regulated Oxidation Resistance of Cu(111). *Nature* **2022**, *603* (7901), 434−438.
(54) Li, X.; Zhu, Q.; Song, K.; Wang, J. Zig-Zag Surface Step Migration and Structure Modulation in Metallic Nanowires. *Mater. Charact.* **2024**, *209*, No. 113752.
(55) Xiao, C.; Lu, B.-A.; Xue, P.; Tian, N.; Zhou, Z.-Y.; Lin, X.; Lin, W.-F.; Sun, S.-G. High-Index-Facet- and High-Surface-Energy Nanocrystals of Metals and Metal Oxides as Highly Efficient Catalysts. *Joule* **2020**, *4* (12), 2562−2598.
(56) Kabalan, L.; Kowalec, I.; Catlow, C. R. A.; Logsdail, A. J. A Computational Study of the Properties of Low- and High-Index Pd, Cu and Zn Surfaces. *Phys. Chem. Chem. Phys.* **2021**, *23* (27), 14649−14661.
(57) Shi, Y.; Lyu, Z.; Zhao, M.; Chen, R.; Nguyen, Q. N.; Xia, Y. Noble-Metal Nanocrystals with Controlled Shapes for Catalytic and Electrocatalytic Applications. *Chem. Rev.* **2021**, *121* (2), 649−735.
(58) Stumpf, R.; Scheffler, M. Ab Initio Calculations of Energies and Self-Diffusion on Flat and Stepped Surfaces of Al and Their Implications on Crystal Growth. *Phys. Rev. B* **1996**, *53* (8), 4958−4973.
(59) Toimil-Molares, M. E.; Balogh, A. G.; Cornelius, T. W.; Neumann, R.; Trautmann, C. Fragmentation of Nanowires Driven by Rayleigh Instability. *Appl. Phys. Lett.* **2004**, *85* (22), 5337−5339.

https://doi.org/10.1021/acs.nanolett.6c01885
Nano Lett. 2026, 26, 8551−8558